Research Square

Preprints are preliminary reports that have not undergone peer review.
They should not be considered conclusive, used to inform clinical practice,
or referenced by the media as validated information.

In-situ microwave modulation of non-equilibrium solidification stress in direct additive manufacturing of ternary eutectic ceramics

Fangyong Niu

niufangyong@dlut.edu.cn

Dalian University of Technology

Xuexin Yu

Weiming Bi

Dalian University of Technology

Jiejie Lan

Dalian University of Technology

Mingchun Zhu

Dalian University of Technology

Dongjiang Wu

Dalian University of Technology

Guangyi Ma

Dalian University of Technology https://orcid.org/0000-0002-4480-7936

Danlei Zhao

Dalian University of Technology

Article

Keywords:

Posted Date: July 3rd, 2026

DOI: https://doi.org/10.21203/rs.3.rs-10069432/v1

License: This work is licensed under a Creative Commons Attribution 4.0 International License.
Read Full License

Additional Declarations: There is **NO** Competing Interest.

In-situ microwave modulation of non-equilibrium solidification stress in direct additive manufacturing of ternary eutectic ceramics

Xuexin Yu[1], Weiming Bi[1], Jiejie Lan[2], Mingchun Zhu[1], Dongjiang Wu[1], Guangyi Ma[1], Danlei Zhao[1], Fangyong Niu[*1]

[1] State Key Laboratory of High-performance Precision Manufacturing, Dalian University of Technology, Dalian 116024, Liaoning, PR China

[2]School of Physics, Dalian University of Technology, Dalian 116024, Liaoning, PR China

***Corresponding author:** Fangyong Niu **Email:** niufangyong@dlut.edu.cn

Abstract

Direct, binder-free additive manufacturing of eutectic ceramics via laser directed energy deposition (LDED) offers immense potential. However, extreme temperature gradients during rapid melting and solidification induce severe thermal stress concentrations, rendering the fabricated components highly susceptible to cracking. Here, we propose an in-situ microwave-laser hybrid additive manufacturing approach for Al_2O_3/YAG/ZrO_2 (AYZ) ternary eutectic ceramics. By leveraging a microwave hybrid heating mechanism featuring external microwave absorbing preheating, laser activated melt pool generation, and internal volumetric heating, we achieve continuous modulation of the thermal field and stress evolution throughout the entire deposition process. The in-situ microwave assistance reduces the maximum first principal stress in the initial deposited layer by 91.7% compared to conditions without microwave assistance. Concurrently, it decreases crack density and maximum crack length by 90.4% and 92.1%, respectively, ultimately enabling the successful fabrication of hundred-millimeter-scale crack-free components. This study establishes a robust in situ thermal stress modulation strategy for highly crack-sensitive oxide eutectic ceramics, providing fundamental insights and technical pathways for the high-quality laser additive manufacturing of complex melt-growth ceramics (MGCs) components.

Introduction

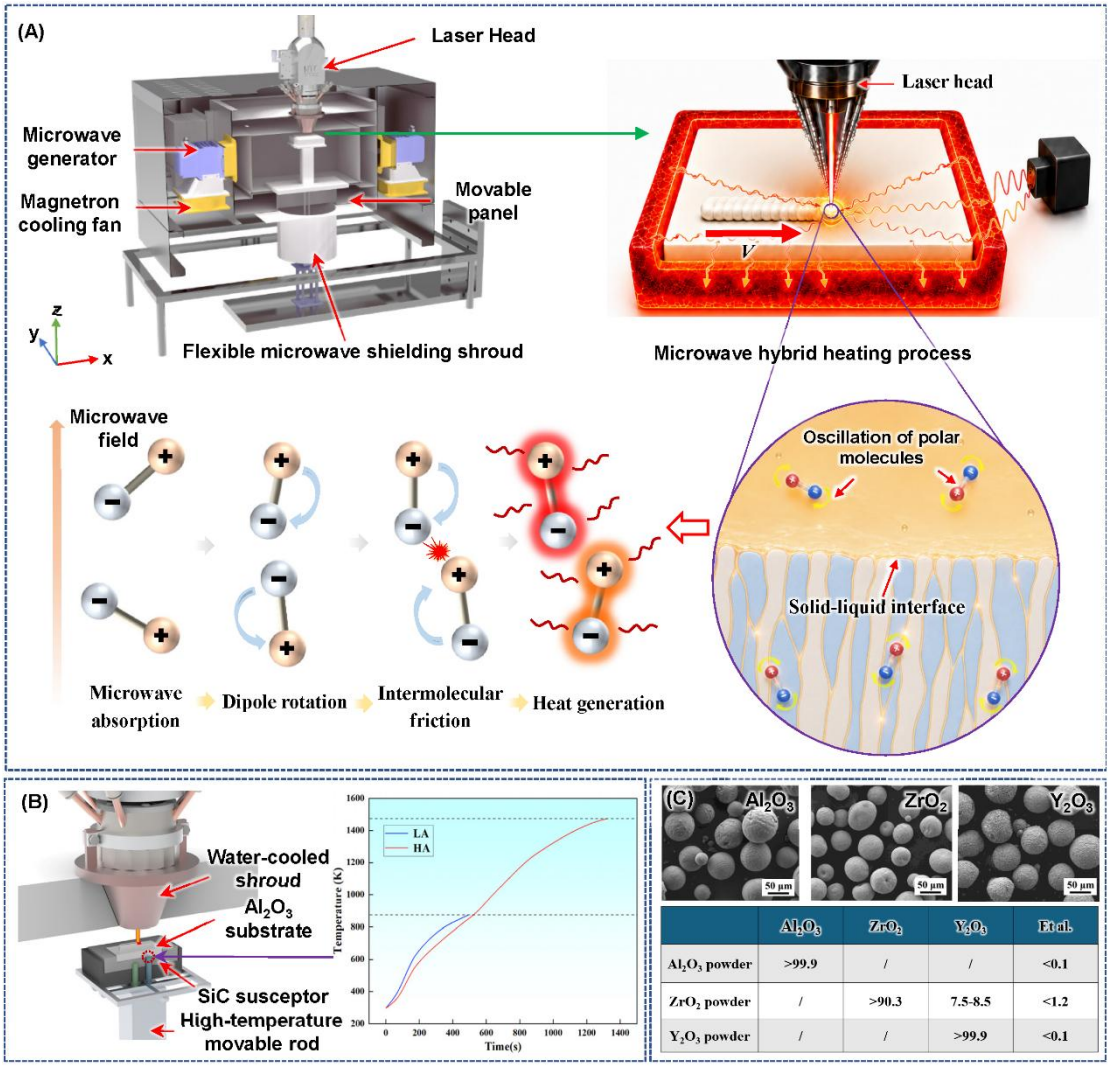
The escalating demands for higher service temperatures and reliability in aerospace and energy systems have driven extensive interest in oxide ceramics, which can maintain microstructural stability and mechanical integrity in extreme oxidizing environments. Melt-growth ceramics (MGCs) are synthesized in situ through direct melt solidification, forming pristine, high-strength

interfaces between crystalline phases. This eliminates the weak amorphous intergranular boundaries typical of conventionally sintered ceramics, enabling MGCs to retain exceptional high-temperature mechanical performance and structural stability even at temperatures approaching their melting points. As a representative oxide MGCs, the Al_2O_3/YAG/ZrO_2 (AYZ) ternary eutectic ceramic is regarded as a highly promising candidate for hot-section components in aero-engines and gas turbines [1-8]. Laser directed energy deposition (LDED) offers a compelling one-step manufacturing pathway from raw powders to complex MGCs components by utilizing high-energy laser beams for in situ melting [9-18]. However, coupling the intrinsic brittleness of ceramics with the rapid melting and solidification dynamics of LDED induces extreme temperature gradients and complex thermal stress evolution. This renders MGCs components highly susceptible to cracking, emerging as the critical bottleneck that restricts their high-quality additive manufacturing and broader engineering applications [19].

Current strategies to mitigate cracking in the LDED of ceramics primarily rely on material design, process optimization, and external field assistance [20-23]. Compositional tuning and microstructural refinement can reduce the intrinsic crack susceptibility of the materials. Meanwhile, process interventions, such as laser remelting and scanning parameter optimization, can partially heal or diminish crack defects [21, 24]. However, these conventional approaches struggle to fundamentally suppress the continuous accumulation of thermal stress during LDED. Furthermore, they are often constrained by narrow processing windows, performance trade-offs, or the unintended introduction of new defects. External field-assisted techniques, such as substrate preheating and ultrasonic vibration, offer promising pathways for active crack control [25, 26]. Nevertheless, their effective domains are largely localized near the substrate. As the deposition height increases, their capability to modulate the thermal and stress fields within the active deposition zone progressively diminishes [27, 28]. Consequently, achieving continuous modulation of the thermal field and stress evolution throughout the entire layer-by-layer deposition process remains the core scientific and technological challenge for suppressing cracking in MGCs.

Inspired by the volumetric heating mechanism in microwave sintering of ceramics [29], we propose an in-situ microwave-assisted LDED approach for fabricating AYZ ternary eutectic ceramics. Our methodology establishes a microwave-laser hybrid modulation mechanism featuring external microwave-absorbing preheating, laser-activated melt pool generation, and internal volumetric heating. During the initial deposition stage, SiC susceptors preferentially absorb microwave energy to provide external thermal compensation for the deposition area. Subsequently, the high-energy laser melts the coaxially fed powders to create a high-temperature melt pool. The resulting extreme heat dramatically enhances the microwave absorption capacity of the constituent ceramic phases, such as Al_2O_3, YAG, and ZrO_2. Consequently, microwave energy is efficiently converted into

internal volumetric heat within the component via dielectric loss [30]. The synergistic coupling of external thermal compensation and internal volumetric heating diminishes temperature gradients and residual tensile stress concentrations throughout the entire deposition process, effectively suppressing crack initiation and propagation. Herein, we systematically investigate the cracking mechanisms in LDED-processed AYZ ternary eutectic ceramics using X-ray computed tomography (CT) three-dimensional reconstruction, fractographic analysis, thermo-mechanical coupling simulations, and crack propagation modeling. Furthermore, we elucidate the fundamental physical mechanisms by which the in-situ microwave-laser hybrid energy field achieves crack suppression.



	Al_2O_3	ZrO_2	Y_2O_3	Et al.
Al_2O_3 powder	>99.9	/	/	<0.1
ZrO_2 powder	/	>90.3	7.5-8.5	<1.2
Y_2O_3 powder	/	/	>99.9	<0.1

Fig. 1. Experimental setup and feedstock materials. (A) Dual-robot collaborative in-situ microwave-assisted LDED system. **(B)** Experimental temperature measurement setup. **(C)** Feedstock materials and their corresponding compositions.

Results

Microwave-enabled suppression of cracking in AYZ eutectic ceramics

In-situ microwave assistance profoundly alters the crack morphology of the LDED-fabricated AYZ

ternary eutectic ceramics (Fig. 2A). Under non-microwave (NM) conditions, the specimens suffer from multiple longitudinal cracks propagating along the deposition direction, with primary cracks displaying a pronounced tendency for continuous extension. The introduction of low-absorption (LA) microwave assistance noticeably reduces both the quantity and dimensions of these primary cracks, indicating an initial suppression of crack initiation and propagation dynamics. Strikingly, by further enhancing the microwave absorption in high-absorption (HA) specimens, macroscopic penetrating cracks are entirely eliminated, successfully yielding crack-free components at the equivalent dimensional scale. These observations unambiguously demonstrate that the efficacy of crack suppression scales directly with the microwave absorption capacity of the component.

Fractographic analysis further elucidates the altered crack propagation dynamics across varying microwave conditions. While longitudinal fractures persist under LA conditions, their surfaces exhibit a distinctly rougher topography compared to the continuous, highly directional fracture texture of NM specimens (Fig. 2B). The emergence of fine fracture ridges and localized roughened zones indicates that low-level microwave absorption, though insufficient to entirely eradicate cracking, effectively retards and deflects the crack propagation path locally. Notably, even under optimal HA conditions, transverse cold cracks can still emerge if the components are removed and rapidly cooled immediately after deposition. The transverse fracture surfaces of these rapidly cooled HA specimens reveal classical brittle cleavage features, including cleavage steps, cleavage planes, river patterns, and secondary cracks (Fig. 2C). These fractographic signatures confirm that the rapid accumulation of residual thermal stress during the cooling phase remains a potent driver for cold cracking. Consequently, while HA microwave assistance fundamentally suppresses longitudinal hot cracking during active deposition, implementing a controlled slow-cooling protocol is equally indispensable to prevent transverse cold cracking during the final cooling stage.

Crack density statistics further quantify the crack suppression efficacy of the microwave assistance. In NM specimens, cracks concentrate predominantly in the lower and mid-lower regions and gradually diminish as the deposition height increases (Fig. 2D). The crack density in LA specimens drops significantly, accompanied by a correspondingly narrowed spatial distribution. Strikingly, the crack density in HA specimens approaches zero across the entire deposition height. Three-dimensional morphological analysis reveals that cracks under NM conditions propagate continuously along the deposition direction with a clear penetrating tendency. Conversely, the primary crack length under LA conditions shortens considerably. Quantitative analysis confirms these visual observations (Fig. 2E). The NM specimens exhibit a crack density of 1.25 mm^{-1} and a maximum crack length of 10.17 mm. Under LA conditions, these values drop to 0.73 mm^{-1} and 4.35 mm, yielding reductions of 41.6% and 57.2%, respectively. The HA conditions further drive these metrics down to 0.12 mm^{-1} and 0.8 mm, achieving remarkable reductions of 90.4% and 92.1%

against the NM baseline. These results unambiguously demonstrate that in-situ microwave assistance simultaneously diminishes crack density and restricts primary crack propagation. Furthermore, coupling HA deposition with a controlled slow-cooling protocol effectively circumvents the formation of both longitudinal penetrating cracks and transverse cold cracks. This synergistic strategy provides a highly viable pathway for the LDED fabrication of high-integrity AYZ ternary eutectic ceramics.

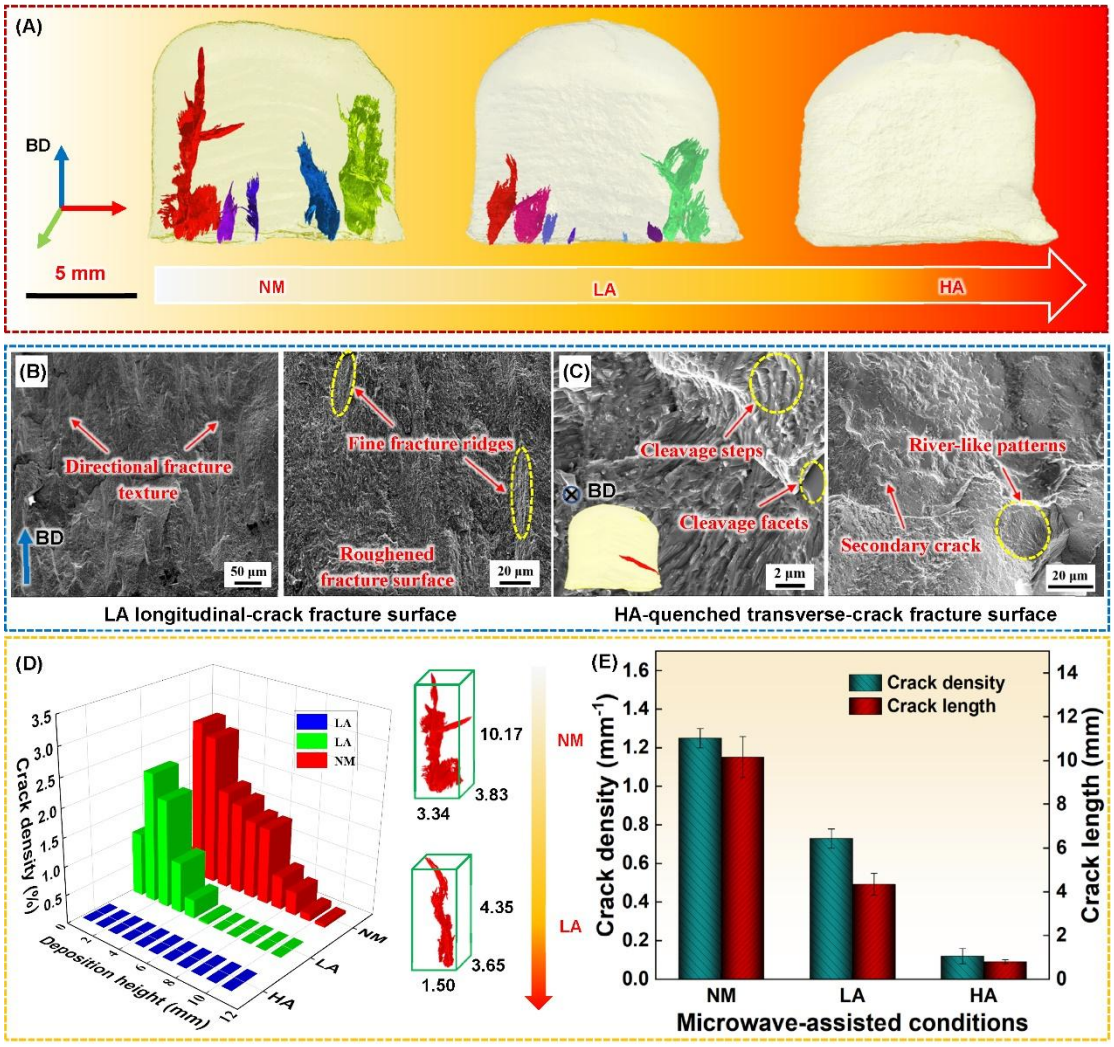


Fig. 2. Comparative crack characteristics of specimens fabricated under varying microwave conditions. (A) Three-dimensional X-ray CT reconstruction of crack morphologies.

(B) Fractographic analysis of longitudinal cracks in the LA specimen.

(C) Fractographic analysis of transverse cold cracks in the HA specimen.

(D) Variation of crack density as a function of deposition height.

(E) Quantitative comparison of overall crack density and maximum crack length.

Mechanism of microwave-regulated crack suppression

In situ microwave assistance fundamentally alters the macro-stress landscape and fracture driving forces during the LDED of AYZ ternary eutectic ceramics (Fig. 3). Finite element analysis reveals a pronounced concentration of X-direction tensile stress at the specimen base and the deposition/substrate interface (Fig. 3A), identifying this interface as a critical zone that spatially mirrors the initiation loci of longitudinal primary cracks. Tracking the first principal stress at the basal feature point F underscores this spatial vulnerability, revealing that under NM conditions, point F undergoes cyclical tensile spikes during layer-by-layer deposition and sustains an elevated stress state that fuels a persistent mechanical driving force for crack nucleation. Elevating the microwave coupling efficiency dramatically suppresses this principal stress accumulation, whereby HA conditions keep the tensile stress at point F completely muted throughout the print, bypassing the severe stress build-up seen in the NM baseline. Volumetric microwave thermal compensation flattens early-stage thermal gradients to throttle longitudinal crack nucleation at its embryonic origin. Beyond quenching crack initiation, the hybrid configuration forcefully disrupts the energy supply required for crack propagation. At the mid-path feature point M (Fig. 3C), the principal tensile stress under NM conditions climbs relentlessly during subsequent layer deposition and exhibits repetitive peaks that provide a continuous mechanical pull to drive the longitudinal crack upward into the specimen core. In sharp contrast, LA conditions noticeably truncate this stress escalation, whereas HA conditions completely neutralize the late-stage tensile build-up. The simulated stress profiles correlate flawlessly with macrostructural observations of primary crack lengths shrinking under LA and disappearing entirely under HA, confirming that in situ microwave coupling acts as a dual-action mechanism that simultaneously smothers the root causes of crack nucleation and starves the kinetic driving forces for upward propagation.

Transverse crack formation, by contrast, originates from a completely distinct stress profile. At the peripheral feature point H (Fig. 3D), the Z-direction stress during the active deposition phase manifests predominantly as compressive or exhibits low-amplitude fluctuations under all processing conditions, indicating a negligible propensity for transverse cracking during active printing. Upon transitioning to the cooling phase, this stress state abruptly shifts to tensile and closely mirrors the trajectory of the first principal stress, signifying that the primary tensile stress driving edge failure stems directly from Z-direction residual tensile stresses. Rapid accumulation of post-deposition residual tensile stress serves as the primary trigger for transverse cracking. Sustaining microwave thermal compensation to enforce a well-regulated slow-cooling protocol post-deposition mitigates this Z-direction stress accumulation under HA conditions, thereby completely preventing transverse cold cracking. Fracture mechanics simulations provide a deeper, energy-based verification of this microwave-enabled crack arrest. Given that longitudinal primary cracks propagate via Mode I

opening, the mechanical driving force along the crack front is explicitly characterized by the stress intensity factor K_I. Compared to the NM baseline, LA conditions markedly lower the crack-front K_I while keeping K_{II} and K_{III} negligibly low (Fig. 3E), confirming that microwave assistance suppresses growth purely by attenuating the opening-mode driving force without altering the intrinsic Mode I failure path. Profiling the continuous propagation reveals that K_I under both NM and LA conditions scales upward initially before declining (Fig. 3F), capturing how the driving force intensifies as the crack enters local stress fields and then decelerates as the front departs from the concentration zone. Crucially, LA conditions keep the K_I profiles for both primary cracks substantially below the NM baseline throughout the entire propagation history, demonstrating that in situ microwave coupling continuously starves the fracture mechanics driving force required to sustain crack advancement.

In situ microwave-enabled crack suppression operates through a tripartite mechanism. Volumetric thermal compensation first minimizes X-direction tensile and first principal stresses at the specimen base, throttling the mechanical driving force for longitudinal thermal crack nucleation at its embryonic origin. Concurrently, microwave coupling curtails both the principal tensile stresses along the propagation pathway and the crack-front K_I levels, forcefully arresting further advancement of nucleated defects. Post-deposition processing under HA conditions, when paired with a well-regulated slow-cooling protocol, mitigates the rapid accumulation of peripheral Z-direction residual tensile stresses to prevent transverse cold cracking. Rather than acting as a superficial external preheating source, the hybrid configuration functions as a persistent thermal stress regulation strategy spanning the entire deposition and cooling history, simultaneously extinguishing the driving forces for both thermal and cold cracks. Ultimately, the microwave-laser hybrid additive manufacturing approach enables the crack-free processing of MGCs components at a hundred-millimeter scale (Fig. 4).

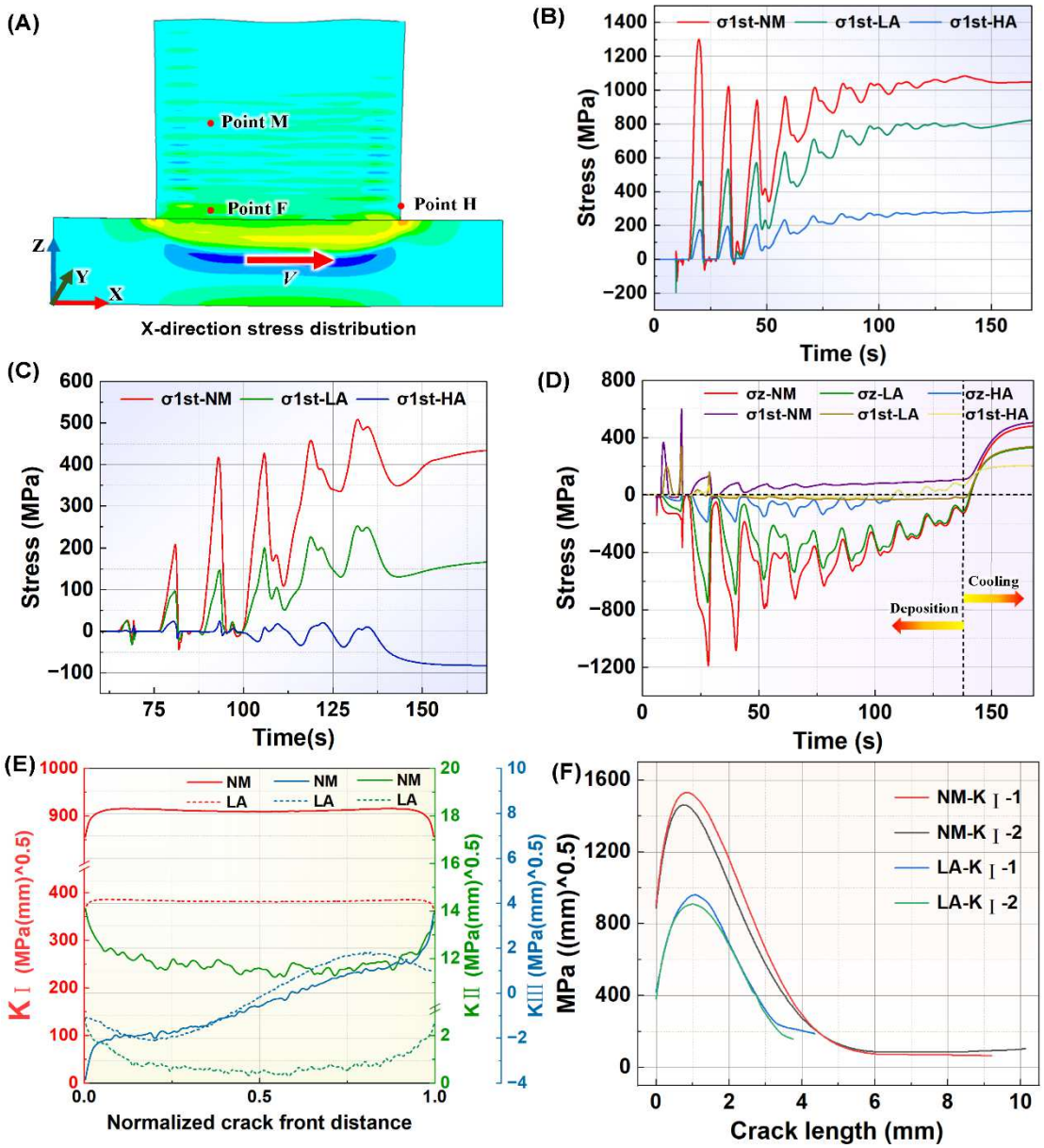


Fig. 3. Thermal-mechanical coupled finite element analysis of stress fields and fracture dynamics under varying microwave-assisted conditions. (A) X-direction stress contours. **(B)** First principal stress evolution over time at basal feature point F. **(C)** First principal stress evolution over time at mid-path feature point M. **(D)** Z-direction principal stress and first principal stress trajectories at peripheral feature point H. **(E)** Stress intensity factor distributions along the initial crack front. **(F)** Mode I stress intensity factor histories during continuous crack propagation.

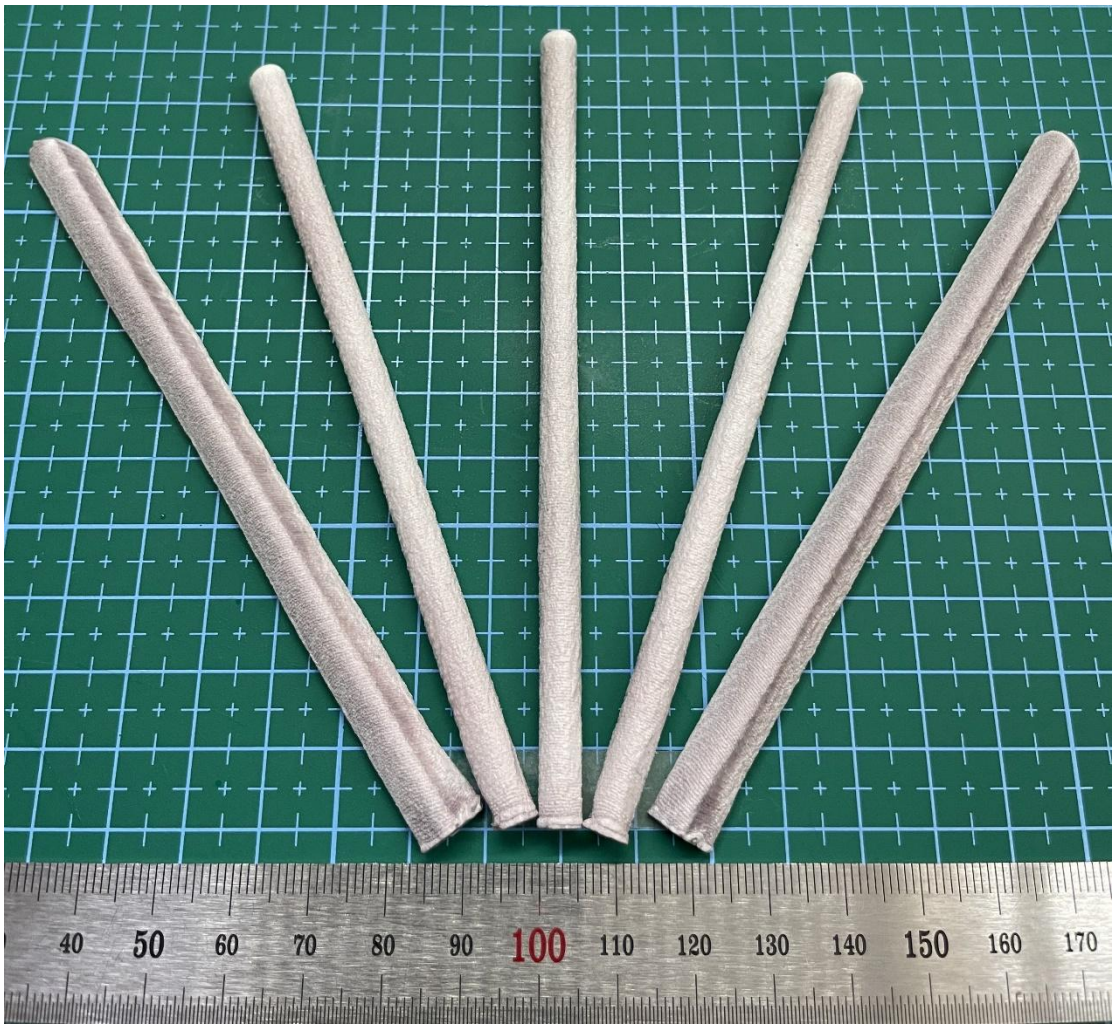


Fig. 4. Macro-morphologies of hundred-millimeter-scale crack-free MGCs components.

Methods

Experiments and methods

The experiments were conducted using a custom-engineered, dual-manipulator collaborative in-situ microwave-assisted laser directed energy deposition (LDED) system. This integrated platform primarily comprised a semiconductor laser system (FCL2000, Cgrs, China), a FWC-300-NewTon coaxial powder feeding deposition head, GP180 and MH12 six-axis vertical articulated robotic manipulators (Yaskawa, Japan), and an RC-PGF powder feeder (Nanjing Lasersurf Technology Co., Ltd., China). The semiconductor laser delivered a maximum output power of 2 kW at a central operating wavelength of 1064 nm. The in-situ microwave auxiliary unit featured a tailored industrial microwave system (XRT-XG) governed by a dedicated control cabinet, wherein the core component was an industrial microwave generator rated at 3 kW with an operating frequency of 2.45 GHz. This configuration satisfied the multi-stage thermal input requirements spanning from initial sample preheating to post-deposition thermal preservation, utilizing a duty-cycle closed-loop regulation

scheme to achieve precise dynamic adaptation to shifting thermal loads. A dedicated cooling fan assembly was incorporated to provide directional thermal management for the magnetron and exhaust heat from the cavity, thereby ensuring prolonged operational stability and microwave frequency coherence. To achieve the relative motion between the substrate and the laser deposition head across the X, Y, and Z axes, a high-temperature mobile support rod was fabricated from 310S stainless steel. This support rod was securely coupled to the GP180 industrial robot via an L-shaped junction plate. Addressing the potential risk of microwave leakage through the bottom aperture of the cavity during motion, a synchronized shielding shroud was deployed at the insertion point of the mobile rod to guarantee system operational safety. Throughout the fabrication process, real-time temperature monitoring and feedback control were executed via K-type thermocouples exhibiting a measurement tolerance of ±1% within a thermal detection range of 273 to 1673 K. To optimize the thermal containment efficacy of the microwave cavity, the interior enclosure was lined with polycrystalline mullite insulation boards capable of withstanding peak temperatures up to 1873 K.

Process conditions and field-coupling strategies

Spherical Al_2O_3 powders with a particle size distribution of 45 to 90 μm (Ya'an Baitu Advanced Materials Co., Ltd., China) along with ZrO_2 and Y_2O_3 powders (Beijing Cespri New Materials Co., Ltd., China) were utilized as the feedstocks. To enhance powder flowability and eliminate moisture-induced agglomeration, all precursor powders were thoroughly dried at 120°C for 4 h prior to deposition. Hot-pressed sintered Al_2O_3 ceramic plates featuring a purity of 95% and dimensions of 150 mm × 100 mm × 15 mm (Shanghai Xiyuan Industrial Co., Ltd., China) were selected as substrates to guarantee excellent interfacial wettability and matching coefficients of thermal expansion between the deposited layers and the substrate. Fundamental to this setup, microwave heating operates as a coupled electro-thermo-chemical process governed by the material-specific absorption and dissipation of electromagnetic energy. Crucially, the dielectric loss of oxide ceramics escalates sharply with rising temperature. Consequently, SiC was introduced as an auxiliary susceptor external heat source to establish a hybrid microwave heating modality. From a microscopic energy conversion perspective, the alternating electric field within the microwave cavity drives a periodic orientation response of the internal polarization domains, defect dipoles, and localized ionic polarization structures. As the external electric field continuously oscillates, these polar entities rotate or vibrate accordingly. Due to the intrinsic phase lag of their response relative to the high-frequency electric field vector, substantial dielectric losses are generated through polarization relaxation, ionic displacement, and interfacial polarization. These multi-scale loss mechanisms effectively convert electromagnetic radiation into internal thermal volume. During the initial heating phase, the SiC susceptor preferentially couples with the microwave field and experiences rapid temperature elevation, acting as an external thermal reservoir that raises the

ambient temperature surrounding the target workpiece. As the temperature crosses critical thresholds, the intrinsic dielectric loss of the ceramic specimen itself amplifies, triggering an enhanced electromagnetic coupling that enables continuous, self-adaptive heating of the material. Prior to the experiments, the Al_2O_3 substrate was positioned atop the SiC susceptor stage, and the hermeticity of the microwave cavity was rigorously verified to prevent radiation leakage. The industrial system was then activated at a forward output power of 3 kW, while a leakage detector concurrently monitored the surroundings to ensure that the radiation intensity remained strictly below the mandated safety threshold of 5 mW/cm^{-2}. Given that the microwave absorption capability of the ceramic workpiece exhibits pronounced temperature dependence, three distinct processing conditions were investigated for comparative analysis. These comprised conventional room-temperature LDED without microwave assistance designated as the no-microwave (NM) condition, low-absorptivity microwave-assisted LDED executed at a substrate preheating temperature of 873 K designated as the low-absorptivity (LA) condition, and high-absorptivity microwave-assisted LDED performed at a substrate preheating temperature of 1473 K designated as the high-absorptivity (HA) condition. The real-time temperature evolution was monitored via a high-temperature thermocouple array attached to the bottom of the substrate. Once the target baseline temperatures of 873 K and 1473 K were reached, the subsequent deposition experiments were initiated under continuous microwave illumination. To isolate the target field-coupling phenomena and eliminate confounding non-target variables, all specimens were fabricated using an identical set of optimized LDED parameters, including a laser power of 250 W, a scanning speed of 2.5 mm s^{-1}, a layer-to-layer vertical increment of 0.4 mm, yielding thin-walled specimens with cross-sectional dimensions of 12 mm × 10 mm on the Al_2O_3 substrates. To ensure the stable operation of the coaxial powder-feeding nozzle, high-purity argon gas was continuously introduced as the carrier and shielding gas throughout the additive manufacturing cycle.

Characterization and analytical methods

The longitudinal cross-sections of the deposited specimens were prepared via standard metallographic procedures. They were ground sequentially using diamond disks from 400 to 3000 grit. Subsequent polishing was executed using a 2.5 μm diamond abrasive paste. Microstructures were characterized using a field-emission scanning electron microscope (FE-SEM, JSM-7900F, JEOL, Japan). Internal cracks within the specimens were detected using a three-dimensional X-ray microscope (ZEISS Xradia 610 Versa, Germany). Three-dimensional reconstructions of the crack networks were performed using Dragonfly visualization software. Quantitative analysis of the crack density and crack length was subsequently conducted within the software environment.

A sequential electromagnetic-thermal-mechanical coupling strategy was developed to reveal the regulatory mechanism of the in-situ microwave field. The numerical model captured the dynamic

evolution of both transient temperature fields and thermal stresses during the LDED process. First, a three-dimensional electromagnetic model was constructed in COMSOL Multiphysics based on the actual experimental configuration. This model incorporated the microwave generator, the resonant cavity, the high-temperature support rod, and the deposition zone. The spatial distribution of the electric field within the cavity was solved. The electromagnetic power loss density and the time-averaged power flow vector around the deposition zone were subsequently extracted. Next, the extracted electromagnetic power loss density was introduced into a thermal-mechanical coupled model as an equivalent volumetric heat source. This microwave thermal input acted simultaneously with the moving laser heat source to solve the transient temperature fields and subsequent thermal stress evolution. This sequential methodology accurately captured the spatially non-uniform thermal characteristics of the microwave field near the deposition zone. Concurrently, it successfully avoided the prohibitive computational costs associated with fully coupled, direct field simulations.

Electromagnetic model and microwave thermal input characterization

A three-dimensional geometric model of the microwave resonant cavity was established based on the actual experimental apparatus. This computational domain primarily comprised the microwave input port, the resonant cavity, the high-temperature support rod, and the local space surrounding the deposition zone. The electromagnetic field was solved in the frequency domain at a fixed operating frequency of 2.45 GHz (Fig. 5(A)). Physically, microwave heating originates from the conversion of electromagnetic energy into volumetric thermal energy via dielectric loss mechanisms. Both the complex permittivity and the electrical conductivity of the constituent materials vary significantly as functions of temperature. Consequently, a frequency-domain solver was implemented to capture the spatial distribution of the electric field within the cavity. The governing wave equation for the electric field vector is formulated as follows:

$$\nabla \times \left(\mu_r^{-1} \nabla \times E \right) - k_0^2 \left(\varepsilon_r - j \frac{\sigma}{\omega \varepsilon_0} \right) E = 0 \tag{1-1}$$

Once the spatial distribution of the electric field was obtained, the electromagnetic power loss density within the material was calculated. This localized variable characterized the volumetric rate of energy conversion from electromagnetic radiation into thermal energy. The specific mathematical expression is formulated as follows:

$$Q_{mw} = \frac{1}{2} \omega \varepsilon_0 \varepsilon'' |E|^2 \tag{1-2}$$

where E is the complex electric field vector, μ_r is the relative permeability, ε_r is the complex

permittivity, k_0 is the free space wavenumber, σ is the electrical conductivity, ε_0 is the vacuum permittivity, and Q is the electromagnetic power loss.

The volumetric heat source Q_{mw} obtained from Eq. (1-2) directly reflected the local deposition intensity of electromagnetic energy around the fabrication zone. Consequently, the resolved value was extracted as an equivalent volumetric heat source for the subsequent thermal analysis. Concurrently, the time-averaged power flow vector was analyzed to characterize the transmission and convergence features of the microwave energy. Such an evaluation effectively mapped the wave propagation directions inside the resonant cavity. The results revealed a pronounced electromagnetic standing wave distribution around the deposition zone. Furthermore, the localized electromagnetic power loss density exhibited distinct non-uniform characteristics, confirming a significant spatial variation in the microwave thermal input. Ultimately, this electromagnetic power loss density field was mapped into the subsequent governing equations for the temperature field. It acted as a persistent microwave background heat input operating simultaneously with the moving laser heat source during the thermal-mechanical coupled simulation of the LDED process.

Thermal-mechanical coupled finite element model

The calculated electromagnetic power loss density field was introduced into the subsequent thermal solver as a steady microwave background heat input. Concurrently, a localized laser power distribution was incorporated to establish the combined heat source condition for the deposition process. During the LDED process, the deposited tracks undergo complex thermal cycles including rapid heating, melting, rapid solidification, and sub-solidus cooling. Consequently, the heat transfer inside the ceramic specimen constitutes a typical non-linear transient heat conduction process. The non-linear governing equation for the transient temperature field is formulated as follows:

$$\rho C_p \frac{\partial T}{\partial t} = \nabla\left(k\nabla T\right) + Q_{laser} + Q_{mw} \tag{1-3}$$

Where ρ is the material density, and C_p is the specific heat capacity. The coefficient k represents the thermal conductivity, while T signifies the transient temperature. Concurrently, Q_{laser} denotes the volumetric laser heat source, and Q_{mv} characterizes the electromagnetic power loss density.

Given that the deposition processes under different operating conditions correspond to distinct preheating states, the initial thermal conditions were defined temperature-dependently.

$$T\left(x, y, z\right) = T_0 \tag{1-4}$$

Where T_0 represents the initial temperature of both the specimen and the substrate. The specific value was determined according to the corresponding experimental conditions.

Regarding the thermal boundary conditions, the heat exchange between the specimen and the ambient environment was governed by both surface convection and thermal radiation. The integrated environmental heat loss condition is formulated as follows:

$$-k\nabla T \cdot n = h(T - T_0) + \varepsilon\sigma(T^4 - T_0^4) \tag{1-5}$$

Where n is the outward normal vector of the boundary surface, and h denotes the convective heat transfer coefficient. The variable ε represents the surface emissivity, while σ signifies the Stefan-Boltzmann constant. The specific value of this constant is approximately 5.67×10^{-8} W·m^{-2}·K^{-4}.

Regarding the mechanical stress field analysis, the calculated temperature field results were imported as thermal load inputs to solve the evolutionary behavior of internal thermal stresses. The localized thermal strain induced by such temperature variations is formulated as follows:

$$\varepsilon_{th} = \alpha(T - T_0) \tag{1-6}$$

Where α represents the linear thermal expansion coefficient. Concurrently, the internal stress distribution and its temporal evolution during the deposition process were solved by incorporating the elastic constitutive relations. For the high-temperature molten zone, the elastic modulus of the material was significantly reduced to characterize the rapid degradation of load-bearing capacity within the molten pool. Such a treatment more reasonably described the thermal stress evolutionary behavior during the sequential deposition process.

Mesh generation and model verification

Mesh density exerts a significant influence on both computational accuracy and solving efficiency. Therefore, a mesh independence analysis was conducted under identical boundary conditions and heat source loads to optimize the grid parameters. The left side of Fig. 5(B) illustrates the specific effects of element size on calculation time, computational error, and storage consumption. The results indicated that larger element sizes led to a marked reduction in both computation time and storage capacity. Concurrently, the simulated temperature errors gradually escalated. The computational efficiency improved most prominently when the element size increased from 0.1 mm to 0.2 mm. Balancing accuracy, efficiency, and resource consumption, a baseline element size of 0.2 mm was ultimately selected for the numerical model. The corresponding meshing result is depicted in the middle section of Fig. 5(B). To verify the reliability of the finite element model, a temperature measurement node was selected on the substrate surface at approximately 4 mm away from the centerline of the deposition track. The transient thermal history during the deposition process was monitored in real time using a thermocouple. The right side of Fig. 5(B) compares the experimentally measured thermal cycle with the simulated results. The comparison demonstrated

excellent agreement in the overall evolutionary trends. Both curves effectively captured the distinctive thermal characteristics of the process, including rapid heating, peak baseline retention, and subsequent slow cooling. Certain local deviations inevitably existed at the peak temperatures. Such discrepancies originated from inevitable fluctuations in the initial preheating state, actual laser energy absorption, and localized heat transfer conditions during the physical experiments. Nevertheless, the global error remained well within an acceptable range. The established finite element model accurately characterized the temperature field evolution during the in-situ microwave-assisted LDED process. Consequently, the validated solver was highly suitable for further analyzing the regulatory effects of the microwave background thermal input on thermal stress distribution and cracking behaviors.

Crack propagation model

The internal stress field calculated by ANSYS was exported to FRANC3D after completing the thermal-mechanical coupled analysis. Subsequently, a 3D crack propagation analysis model was established to investigate the crack behaviors during the in-situ microwave-assisted LDED process. The prior thermal-mechanical stress field served as the initial loading condition for crack propagation. Such a setup realized a sequentially coupled analysis from the temperature and stress fields to the crack behaviors. The insertion location of the initial crack was determined based on the stress concentration characteristics from the coupled simulation. Concurrently, experimentally observed crack morphologies were incorporated to guide the placement.

High-stress zones were identified on the near-symmetric sides of the first two deposited tracks. Therefore, two primary cracks were pre-inserted into both sides of the cladding layer. These initial configurations represented the sites most susceptible to propagation during deposition. The geometry and dimensions of the initial cracks were set equivalently based on real specimen characteristics. Such equivalent modeling ensured a reliable agreement with the experimental crack morphologies. The mesh surrounding the crack front was locally refined during the analysis. Specialized crack-front singular elements were utilized to capture the stress singularity near the crack tip. Fracture parameters along the crack front were resolved using the M-integral method. Consequently, the Mode I, Mode II, and Mode III stress intensity factors were obtained for various nodes. The resolved intensity factors characterized the localized driving forces for crack propagation at different positions. The M-integral expression is formulated as follows:

$$M = \int_{\tau} (W x_i n_i - T_j u_{j,i} x_i) ds \tag{1-7}$$

Where τ represents the integration path enclosing the crack tip, and W denotes the strain energy density. The term T_j signifies the traction components along the integration path, while $u_{j,i}$ indicates the displacement gradient vector. Concurrently, n_i represents the direction cosines of the outward normal line, and x_i defines the coordinate components.

On this basis, step-by-step propagation simulations of the pre-inserted primary cracks were executed using FRANC3D. During each incremental step, the crack-front morphology was updated according to the calculated fracture parameters. Concurrently, the localized mesh was automatically reconstructed to achieve a continuous solution for the crack growth process. Such a model enabled a comprehensive analysis of the stress intensity factor distributions along the crack front. Their evolutionary characteristics were systematically investigated as functions of both the propagation step and crack length. Ultimately, these simulation findings provided a solid numerical foundation to reveal the cracking mechanisms of the specimen. The quantitative results also clarified the regulatory effects of the microwave-assisted process on crack propagation behaviors.

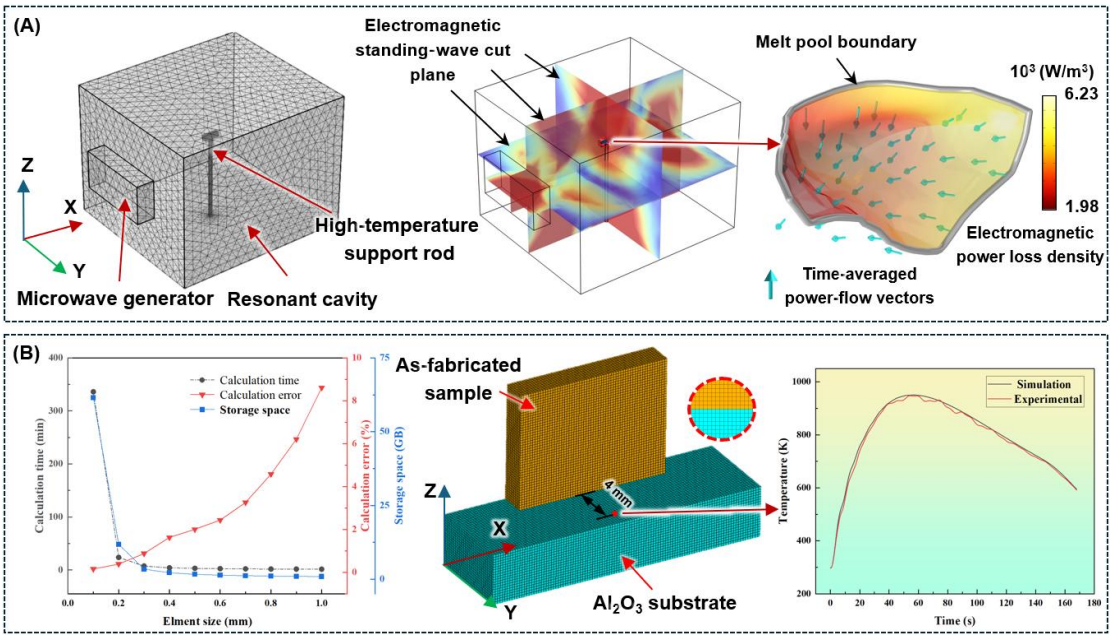


Fig. 5 Overview of the electromagnetic-thermal-mechanical coupled finite element model. (A) Determination of the electromagnetic power loss density. (B) Thermal-mechanical coupled finite element model and experimental temperature verification.

References

[1] Bose S., Akdogan E. K., Balla V. K., et al. 3D printing of ceramics: Advantages, challenges, applications, and perspectives[J]. Journal of the American Ceramic Society, 2024, 107(12): 7879-7920.

[2] Llorca J., Orera V. M. Directionally solidified eutectic ceramic oxides[J]. Progress in Materials Science, 2006, 51(6): 711-809.

[3] Shen Z., Su H., Yu M., et al. Unveiling exotic multi-scale microstructure transformation and crack formation mechanisms in eutectic ceramic composite by laser powder bed fusion[J]. Composites Part B-Engineering, 2025, 288: 12.

[4] Zhao D., Su H., Lu B., et al. Ultra-high strength micro-nano quasi-monocrystalline $Al_2O_3/Y_3Al_5O_{12}/ZrO_2$ ternary eutectic ceramics processed by high-speed directional solidification[J]. Journal of the European Ceramic Society, 2025, 45(13): 117485.

[5] Waku Y., Nakagawa N., Wakamoto T., et al. A ductile ceramic eutectic composite with high strength at 1873 K[J]. Nature, 1997, 389(6646): 49-52.

[6] Vakhshouri M., Talimian A., Najafzadehkhoee A., et al. Fabrication of Al_2O_3-$Y_3Al_5O_{12}$-ZrO_2 composites by single-step spark plasma sintering[J]. Journal of the European Ceramic Society, 2025, 45(10): 117358.

[7] Hao S., Su H., Zhao D., et al. Complex shaped Al_2O_3/YAG/ZrO_2 eutectic ceramics with excellent high temperature mechanical properties printed by vat photopolymerization[J]. Additive Manufacturing, 2025, 101: 104703.

[8] Xiong Z., Zhang K., Liao W., et al. In - situ synthesis of high-entropy $Al_2O_3/RE_3Al_5O_{12}/ZrO_2$ ceramic by laser powder bed fusion with exceptional properties[J]. Journal of Advanced Ceramics, 2024, 13(12): 2004-2020.

[9] Wang X., Zhang W., Xian Q., et al. Preparation and microstructure of large-sized directionally solidified $Al_2O_3/Y_3Al_5O_{12}$ eutectics with the seeding technique[J]. Journal of the European Ceramic Society, 2018, 38(16): 5625-5631.

[10] Lee J. H., Yoshikawa A., Murayama Y., et al. Microstructure and mechanical properties of $Al_2O_3/Y_3Al_5O_{12}/ZrO_2$ ternary eutectic materials[J]. Journal of the European Ceramic Society, 2005, 25(8): 1411-1417.

[11] Balla V. K., Bose S., Bandyopadhyay A. Processing of bulk alumina ceramics using laser engineered net shaping[J]. International Journal of Applied Ceramic Technology, 2008, 5(3): 234-242.

[12] Fan Z., Tan Q., Kang C., et al. Advances and challenges in direct additive manufacturing of dense ceramic oxides[J]. International Journal of Extreme Manufacturing, 2024, 6(5): 36.

[13] Zhao D., Bi G., Chen J., et al. A critical review of direct laser additive manufacturing ceramics[J]. International Journal of Minerals Metallurgy and Materials, 2024, 31(12): 2607-2626.

[14] Jiang H., Su H., Yu M., et al. Insights into the influence of powder particle shape on forming process and mechanical properties of Al_2O_3 ceramic fabricated by laser directed energy deposition[J]. Additive Manufacturing, 2024, 81: 12.

[15] Jiang H., Su H., Yu M., et al. LDED-induced pore defects in $Al_2O_3/GdAlO_3/ZrO_2$ eutectic ceramics: Influence of specimen geometry on pore evolution mechanism[J]. Journal of Materials Science & Technology, 2026, 269: 295-305.

[16] Yu X., Wu D., Feng X., et al. One-step additive manufacturing of melt-growth porous ceramics by laser directed energy deposition[J]. Journal of the European Ceramic Society, 2024, 44(15): 5.

[17] Yao J., Su H., Jiang H., et al. Enhanced 3D printing in large-size $Al_2O_3/GdAlO_3/ZrO_2$ eutectic ceramics directly by laser directed energy deposition based on an oscillation process[J]. Journal of Manufacturing Processes, 2025, 155: 747-759.

[18] Li X., Su H., Dong D., et al. Strategic design and functional evaluation of oligomer components in vat photopolymerization 3D printing of alumina ceramics[J]. Journal of the European Ceramic Society, 2025, 45(16): 10.

[19] Liu Z., Ma C., Chang Z., et al. Advances in crack formation mechanism and inhibition strategy for ceramic additive manufacturing[J]. Journal of the European Ceramic Society, 2023, 43(12): 5078-5098.

[20] Yu X., Wu D., Bi W., et al. Direct additive manufacturing of Al_2O_3 -TiCp functionally graded ceramics by laser-directed energy deposition[J]. Journal of the American Ceramic Society, 2024, 107(5): 3522-3533.

[21] Yu S., Su H., Jiang H., et al. Surface remelting strategy for enhancing forming quality in laser directed energy deposition of $Al_2O_3/GdAlO_3/ZrO_2$ eutectic ceramics: Defect suppression and microstructure evolution[J]. Journal of Advanced Ceramics, 2026, 15(1): 9221198.

[22] Su H. J., Zhang J., Liu L., et al. Rapid growth and formation mechanism of ultrafine structural oxide eutectic ceramics by laser direct forming[J]. Applied Physics Letters, 2011, 99(22): 3.

[23] Su H., Ren Q., Zhang J., et al. Microstructures and mechanical properties of directionally solidified $Al_2O_3/GdAlO_3$ eutectic ceramic by laser floating zone melting with high temperature gradient[J]. Journal of the European Ceramic Society, 2017, 37(4): 1617-1626.

[24] Fan Z., Tan Q., Yuan L., et al. Solute-induced grain refinement for crack suppression in laser additive manufactured ceramics[J]. Acta Materialia, 2025, 292: 12.

[25] Hu Y., Ning F., Cong W., et al. Ultrasonic vibration-assisted laser engineering net shaping of ZrO_2-Al_2O_3 bulk parts: Effects on crack suppression, microstructure, and mechanical properties[J]. Ceramics International, 2018, 44(3): 2752-2760.

[26] Liu H., Su H., Shen Z., et al. Preparation of large-size $Al_2O_3/GdAlO_3/ZrO_2$ ternary eutectic ceramic rod by laser directed energy deposition and its microstructure homogenization mechanism[J]. Journal of Materials Science & Technology, 2021, 85: 218-223.

[27] Wu D., Liu H., Lu F., et al. Al_2O_3-YAG eutectic ceramic prepared by laser additive

manufacturing with water-cooled substrate[J]. Ceramics International, 2019, 45(3): 4119-4122.
[28] Yan S., Wu D., Niu F., et al. Effect of ultrasonic power on forming quality of nano-sized Al_2O_3-ZrO_2 eutectic ceramic via laser engineered net shaping (LENS)[J]. Ceramics International, 2018, 44(1): 1120-1126.
[29] Chen Y. Q., Wang Y. X., Zhang F., et al. Preparation of Special Ceramics by Microwave Heating : a Review[J]. Journal of Inorganic Materials, 2022, 37(8): 841-852.
[30] Yu X., Bi W., Yin S., et al. In-situ microwave - laser hybrid additive manufacturing of nano Al_2O_3/YAG/ZrO_2 ternary eutectic melt-growth ceramics: control of microstructural homogeneity and high densification[J]. International Journal of Extreme Manufacturing, 2026, 8(3): 35005.

Acknowledgments

This work was funded by the National Natural Science Foundation of China (No. 52375312).

Author contributions

Xuexin Yu: Conceptualization, Methodology, Investigation, Visualization, Formal analysis, Writing - original draft. **Weiming Bi**: Investigation, Experiments, Writing - review & editing. **Jiejie Lan**: Writing - review & editing. **Mingchun Zhu**: Investigation, Experiments. **Dongjiang Wu**: Investigation, Experiments, Writing - review & editing, Project administration, Funding acquisition, Supervision. Writing - review & editing. **Guangyi Ma**: Resources, Funding acquisition. **Danlei Zhao**: Resources, Funding acquisition. **Fangyong Niu**: Conceptualization, Methodology, Formal analysis, Investigation, Writing - review & editing, Funding acquisition.

Competing interests

The authors declare that they have no known competing financial interests or personal relationships that could have appeared to influence the work reported in this paper.